Construction and Building Materials 403 (2023) 133068

Contents lists available at ScienceDirect

Construction and Building Materials

journal homepage: www.elsevier.com/locate/conbuildmat

Hygro-thermo-mechanical model for concrete pavement from an early age to a long-term performance

Jakub Veselý [a,b,*], Vít Šmilauer [a]

[a] Department of Mechanics, Faculty of Civil Engineering, Czech Technical University in Prague, Czech Republic
[b] Department of Road Structures, Faculty of Civil Engineering, Czech Technical University in Prague, Czech Republic

ARTICLE INFO

Dataset link: http://dx.doi.org/10.17632/4kmfsjz5p7.1, Hygro-thermo-mechanical model for concrete pavement from an early age to a long-term performance (Original data)

Keywords:
Concrete pavement
Finite element analysis
Moisture transport
Drying
Temperature
Hydration

ABSTRACT

A new 3D hygro-thermo-mechanical model for a single concrete pavement slab is formulated with the objective to capture slab behavior from casting to long-term drying. Strain and temperature data from five-year continuous monitoring system served for calibration and validation. Four simulated scenarios show temperature analysis after concrete casting, cyclic temperature effect and stress/strain response for traffic load and long-term drying. The results show that slab drying leads to the highest principal tensile stress on the surface and induces surface cracking when combined with temperature and traffic effects.

1. Introduction

Concrete pavements present a proven solution for highways and airports due to their ability to withstand high mechanical loads with a long service life compared to bituminous alternatives [1]. The effects of wheel load, temperature and moisture generally need attention since they have an impact on stress, strain, deformations and service life [2]. Thermal boundary conditions, hydration heat and autogenous shrinkage were found critical for early-age performance [3], amplified with rapid cooling with crack formation [4,5]. Several measures can mitigate crack formation, from minimizing the temperature gradient [6], choosing a suitable concrete mix, avoiding morning casting [7] or controlling early water evaporation [8].

The evolution of the pavement temperature field is critical for pavement design and is the consequence of air temperature, solar radiation, hydration, subsoil temperature or wind [9–11]. In several cases, the stresses from temperature effects surpass the stresses from the traffic load [12]. The effect of various factors has been reflected in the evolution of mechanical pavement models, departing from analytical solutions to numerical models, including also multiphysical effects [13]. A brief review follows.

The first analytical solutions for concrete pavements were introduced by Westergaard [14,15]. His theories treated the concrete pavement as a plate on a bed of springs, adopting several restrictive assumptions, e.g. single slab, single wheel load, homogeneous concrete, semi-infinite foundation, zero slab weight, linear temperature profile across the thickness. Some of these restrictive assumptions were gradually eliminated by Westergaard himself or the others. One of the latest semi-analytical solutions for concrete pavements [16] treats the pavement slab as the Euler–Bernoulli beam on an improved Winkler subsoil. Each crack is represented by a set of tension/compression, shear and rotation elastic springs, splitting the beam into interacting segments.

The first published numerical stress analysis of concrete pavements is dated back to 1980s, where Huang and Wang developed the KENWINK 2D finite element software, where the concrete slab is represented by a thin plate on a Winkler foundation [17]. The model uses a thermo-mechanical approach with linear temperature profile considering the real dead weight of the concrete slab, multiple wheel loads and day/night temperature effects. The ILLI-LAYER finite element software [18], implementing a multi layered system for the pavement, allowed handling non-linear temperature as a piece-wise constant temperature profile, further evolution was published by Choubane and Tia [19].

Another 2D finite element program ILLI-SLAB [20], is based on the classical theory of a thick plate resting on a Winkler foundation that can be used to perform analysis for pavements with joints, dowel bars or cracks [20]. Similar 2D software applications use slightly different

* Corresponding author at: Department of Mechanics, Faculty of Civil Engineering, Czech Technical University in Prague, Czech Republic.
E-mail addresses: jakub.vesely.2@fsv.cvut.cz (J. Veselý), vit.smilauer@cvut.cz (V. Šmilauer).

https://doi.org/10.1016/j.conbuildmat.2023.133068
Received 23 January 2023; Received in revised form 16 August 2023; Accepted 19 August 2023
Available online 2 September 2023

approaches to the load transfer between the pavement slabs. Namely WESLIQID [21], J-SLAB [22] or KENSLABS [23], which allows two layers of the slab and different subsoil models (Winkler, Boussinesque, Burmister).

Advanced pavement analysis is connected with general finite element software, e.g. Abaqus, Ansys, allowing the incorporation of various factors into the analysis. The following papers focus on topics in load transfer, dowel bar efficiency, dowel bar misalignment effect or thermal loading influence on load transfer [24–28]. The coupling effects of temperature and traffic loads were analyzed [29], using a slab on an elastic foundation with a perfect interface between the slab and the foundation to inspect the effect of slab thickness and subsoil stiffness.

The next category of models recognized the effects of moisture changes, taking into account autogenous shrinkage, drying shrinkage and its effect on creep and possibly early microcracks [30]. In addition, moisture gradients generate differential shrinkage between the top and the bottom, leading to warping [31,32], while stress relaxation plays a beneficial role [33].

Thermo-hygro-mechanical models have been elaborated for general concrete structures [34–37] with different levels of complexity, implementing either staggered or fully-coupled solution strategies. Different versions for concrete pavements were implemented by several authors; Dong et al. [38] proposed moisture transport, heat transport with the MPS mechanical model to inspect the concrete pavement under service life, while Malárics et al. [39] solved thermal, moisture, traffic and ASR effects separately and used the superposition principle.

The objective of the paper focuses on the overall performance of a single concrete slab from the beginning of hydration to the long-term performance. The geometry uses a 3D representation of a single rectangular concrete slab without dowel bars, resting on a Winkler–Pasternak foundation. A staggered solution strategy uses gradual solving of weakly-coupled hygro-thermo-mechanical submodels. The calibration and validation stems from a long-term slab monitoring on a pilot highway section.

2. Formulation of thermo-hygro-mechanical model

The thermo-hygro-mechanical model solves the transport of heat, moisture and mechanical behavior. The staggered solution strategy is adopted, solving transport transient problems first and passing transient fields to the mechanical problem in a unidirectional way. Such an approach allows incorporating directly the effect of temperature and humidity on mechanical behavior. The models were implemented in OOFEM, open-source and object-oriented software for finite element analysis [40].

2.1. Model for heat transport

The transient heat transport is described with the following balance equation

$$-\nabla^T \boldsymbol{q}(\boldsymbol{x}) + Q(\boldsymbol{x},t) = \rho(\boldsymbol{x})c(\boldsymbol{x})\frac{\partial T(\boldsymbol{x},t)}{\partial t}, \tag{1}$$

where $\boldsymbol{q}(\boldsymbol{x})$ is the heat flux, originating from Fourier's law or boundary conditions, $Q(\boldsymbol{x},t)$ is the heat source capturing hydration heat, $\rho(\boldsymbol{x})$ is the concrete density, $c(\boldsymbol{x})$ is the specific heat capacity and $T(\boldsymbol{x},t)$ is the unknown temperature field. Three boundary conditions are used in the normal direction of the flow q_n

- Neumann boundary condition $q_n = -kq_s$ representing heat flux as an absorption from the solar irradiance q_s, taking $k = 0.5$ for concrete,
- Newton (convection) boundary condition $q_n = h(T - T_\infty)$ with the heat transfer coefficient h and the ambient air temperature T_∞,
- Stefan–Boltzmann boundary condition $q_n = \varepsilon\sigma(T^4 - T_\infty^4)$ with the thermal emissivity $\varepsilon = 0.85$ for concrete and the ambient air temperature T_∞. The condition helps mainly to cool down the slab during night by emitting thermal radiation.

The released heat rate at a material point, $Q(\boldsymbol{x},t)$, is obtained from numerical integration of the four-parametric affinity hydration model in every integration point as

$$\frac{\mathrm{d}\alpha}{\mathrm{d}t} = \left[B_1\left(\frac{B_2}{\alpha_\infty} + \alpha\right)(\alpha_\infty - \alpha)\exp\left(-\bar{\eta}\frac{\alpha}{\alpha_\infty}\right)\right] \times \exp\left[\frac{E_a}{R}\left(\frac{1}{T_0} - \frac{1}{T}\right)\right], \quad \alpha(t=0) = 0, \tag{2}$$

$$Q(\boldsymbol{x},t) = Q_{pot} m_c \frac{\mathrm{d}\alpha}{\mathrm{d}t}, \tag{3}$$

where Q_{pot} is potential hydration heat at complete cement hydration, m_c is the cement mass in a unit concrete volume, $B_1, B_2, \alpha_\infty, \bar{\eta}$ are four parameters of the affinity model, α is the degree of hydration, and T_0 is the reference temperature 298.15 K [40]. Scaling to different temperatures is based on the Arrhenius equation with the activation energy E_a.

The concrete thermal conductivity, λ, generally decreases during hydration. The dependence on the degree of hydration is taken as

$$\lambda = \lambda_0(1.33 - 0.33\alpha). \tag{4}$$

2.2. Model for moisture transport

A nonlinear moisture transport model describes concrete as a single-fluid medium with the governing equation

$$k(h)\frac{\partial h}{\partial t} = \nabla \cdot [c(h)\nabla h], \tag{5}$$

where h is the dimensionless pore relative humidity, $k(h)$ (kg/m^3) is the humidity-dependent moisture capacity $k(h) = \frac{\partial w}{\partial h}$ (in the case of a linear sorption isotherm, moisture capacity becomes constant $k(h) = k_1$), $c(h)$ (kg/m/d) is the moisture permeability in the Bažant–Najjar's form

$$c(h) = c_1\left(\alpha_0 + \frac{1-\alpha_0}{1 + \left(\frac{1-h}{1-h_c}\right)^n}\right). \tag{6}$$

Only the Newton (convection) boundary condition is used in the form $q_n = \beta(h - h_\infty)$ with the moisture transfer coefficient β (kg/m$^2\cdot$ s), which can be calculated according to [41,42] as

$$\beta = (6.028 \cdot 10^{-7} \cdot w/c - 2.378 \cdot 10^{-7}) \cdot k_1 \tag{7}$$

2.3. Mechanical model

The mechanical model encompasses the slab, 2D subsoil and interface elements. The concrete slab uses a viscoelastic material model for concrete with ageing based on the microprestress solidification theory (MPS) [43]. The slab is placed on elastic 2D subsoil described by the Winkler–Pasternak model. The interaction between the slab and subsoil bodies is secured by interface elements with a bilinear elastic material law.

2.3.1. Linear viscoelastic material model for creep and shrinkage

A constitutive model for creep and shrinkage originates from the B3 model [44] extended with the MPS formulation [43]. The rheological scheme in Fig. 1 shows a non-aging asymptotic elastic spring, solidifying Kelvin chain, aging dashpot, shrinkage strain, and thermal strain. The viscosity η_f in the dashpot ε_f depends on the evolution of the microprestress. All these units are connected in series, manifesting total strain decomposition into individual components.

The governing equation for the MPS theory [45] reads

$$\dot{\eta}_f + \frac{k_3}{T_0}\left|T\frac{\dot{h}}{h} - \kappa_T\dot{T}\right|\eta_f^{\frac{p}{p-1}} = \frac{\psi_S}{q_4}, \tag{8}$$

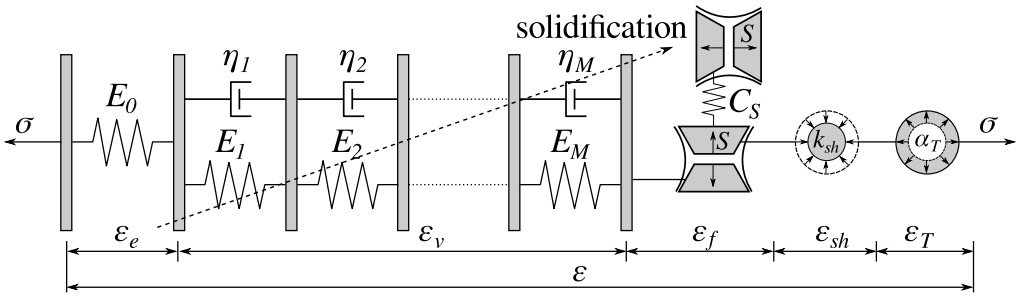

Fig. 1. Rheological scheme of the MPS model.

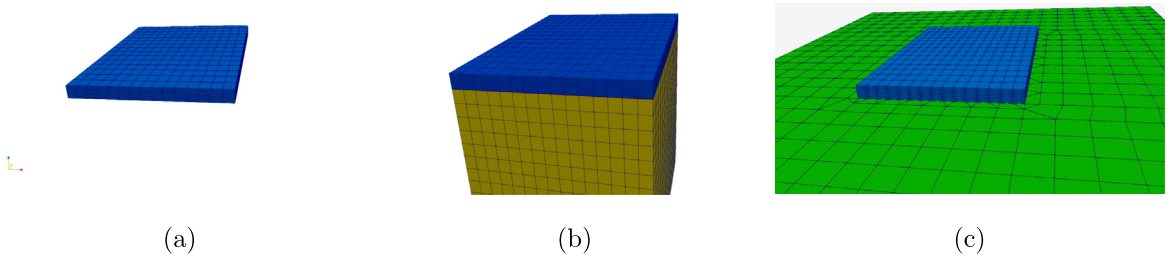

Fig. 2. Meshes for (a) the moisture sub-model (b) the thermal sub-model and (c) the mechanical sub-model.

Fig. 3. Installation of the monitoring system. Prior to the casting, gauges were protected under the orange covers, assembled later to correct heights and filled back with concrete.

where k_3 is a parameter controlling sensitivity to moisture and temperature change, p is a dimensionless material parameter influencing the size effect (for $p > 100$ the size effect disappears), ψ_S is a temperature and humidity dependent factor, q_4 is a material parameter of the B3 model, T is the current temperature, and T_0 is the reference temperature. The basic creep in the MPS theory is influenced by the same four parameters $q_1 - q_4$ as in the B3 model, which are computed from the 28 day mean cylinder compression strength $\overline{f}_c$, the cement content c_c, the water/cement ratio w/c and the aggregate/cement ratio a/c.

The effect of moisture changes is expressed in an incremental form as

$$\dot{\varepsilon}_{sh,d} = k_{sh}\dot{h}, \tag{9}$$

where the drying shrinkage rate $\dot{\varepsilon}_{sh,d}$ is defined using the shrinkage coefficient k_{sh}. The autogenous shrinkage $\varepsilon_{sh,au}$ is taken from the B4 model [46]

$$\varepsilon_{sh,au} = \varepsilon^{\infty}_{sh,au}\left[1 + (\tau_{au}/t_e)^{\alpha}\right]^{r_t}, \tag{10}$$

where $\varepsilon^{\infty}_{sh,au}$ is the ultimate value of autogenous shrinkage strain, τ_{au} is the shrinkage halftime, t_e is the equivalent time, α, r_t are parameters [46].

Depending on the solved problem, several simplifications are introduced, e.g. the short-term static test and cyclic temperature scenarios use only constant time-independent stiffness of mature concrete.

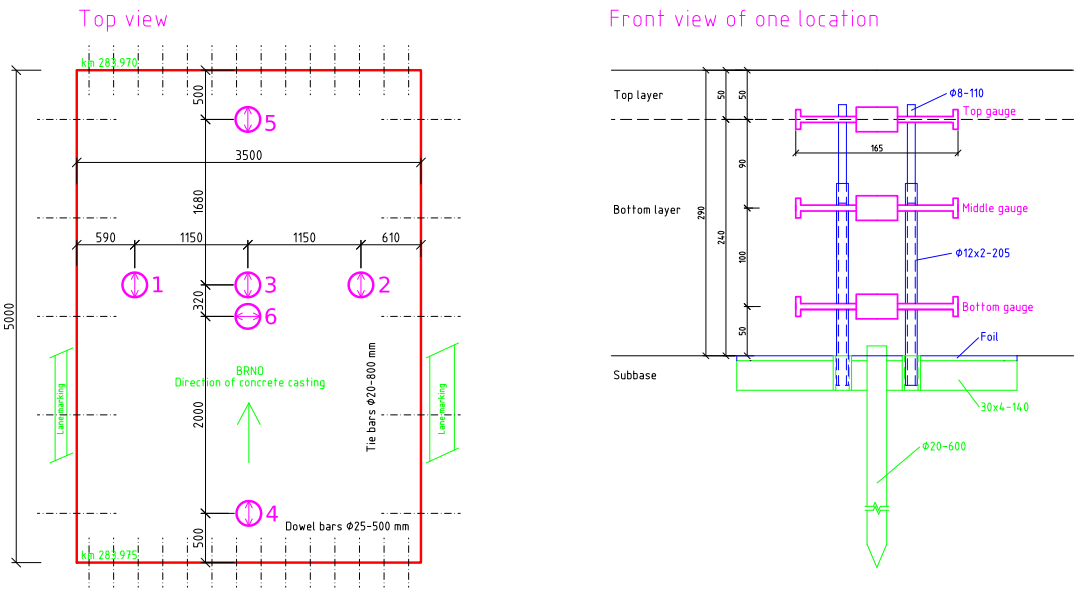

Fig. 4. Top view of the monitored concrete slab with gauges orientations and front view of one location.

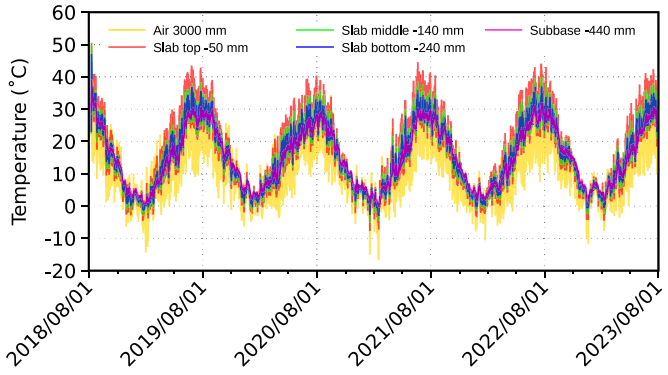

Fig. 5. Temperature evolution at selected gauges, including air and sub-base temperatures.

2.3.2. Winkler–Pasternak subsoil model

Elastic subsoil is considered as a 2D Winkler–Pasternak model, capturing normal and shear stiffness with c_1 and c_2 parameters [47–49]. The governing equation reads

$$f(z) = c_1 w(z) - c_2 \frac{\partial^2 w(z)}{\partial z^2}, \tag{11}$$

where $f(z)$ is the surface normal load and $w(z)$ is the deflection in the z direction. The shear stiffness c_2 controls load distribution outside the loaded area.

2.3.3. Interface elements

The interface elements allow separation between the slab and the subsoil, eliminating tensile stress. Both the 3D slab mesh and the 2D subsoil mesh have coinciding nodes at the interface. The traction-separation law takes the form

$$t_n = k_n \delta, \tag{12}$$

$$k_n = k \quad \text{in compression}, \tag{13}$$

$$k_n = 0.01k \quad \text{in tension}, \tag{14}$$

where δ is the displacement between two nodes, positive in the separation mode and k is the stiffness in compression. Shear stiffness is assumed as zero. Interface elements lead generally to a slower convergence or even a convergence loss hence it is important to use a reasonably short time step to induce a gradual slab separation and stiffness change according to Eqs. (12)–(14).

3. Results and discussion

Simulations and validations are based on a long-term monitoring system of a single concrete slab $3.5 \times 5.0 \times 0.29$ m. Fig. 2 shows the meshes used for transport and mechanical sub-problems.

The meshes for particular sub-problems contain

- Moisture transport: 2250 3D linear brick elements,
- Heat transport: 5850 3D linear brick elements, 2250 for concrete and 3600 for subsoil,
- Mechanical behavior: 1350 3D quadratic 20 node brick elements for concrete, 735 interface elements, 712 2D elastic linear subsoil elements.

3.1. Long-term monitoring system

A pilot highway project started in 2017, testing slow-hardening cement for long-life concrete pavement [50,51]. The pavement was cast on the D1 highway Přerov-Lipník nad Bečvou, the Czech Republic, in the length of 31.1 lane km, the altitude is around 200 meters above the sea level. Casting started 07/2018 and finished 09/2019, the opening to the public occurred Dec 12, 2019. The slow-hardening binder, corresponding to CEM II/B-S 42.5 N, was made from standard road cement and ground granulated blast furnace slag, particularly mixing 75% CEM I 42.5 R(sc) + 25% GGBFS SMŠ 400 in the concrete plant [50].

A long-term monitoring system was designed and installed in one concrete pavement slab with the dimensions of $3.5 \times 5.0 \times 0.29$ m. The system records temperature and strains at six measuring locations, see Figs. 3, 4. Placing two layers of concrete required hiding the gauges under covers, excavate them after casting of the bottom layer, assemble them to the correct heights, fill the space back with concrete and cast the top layer, see Fig. 3. At the end, six locations were monitored with three gauges in each, yielding 18 strain and temperature data from the slab. In addition, one thermal gauge was placed 150 mm under the pavement in order to deliver the sub-base temperature. Ambient air temperature and solar radiation sensors were installed as well.

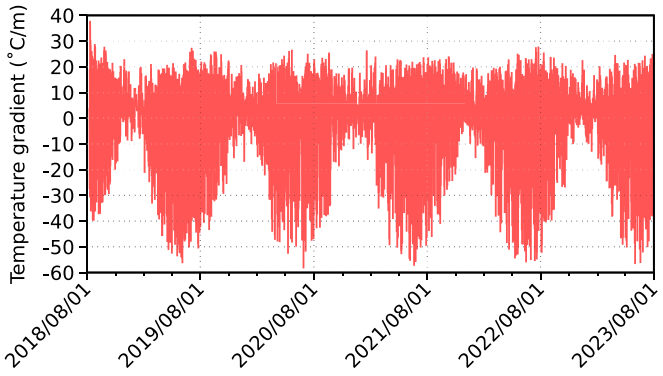

Fig. 6. Temperature gradient over the slab thickness.

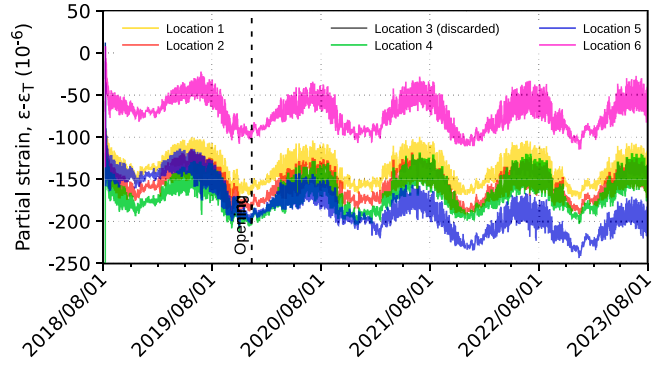

Fig. 7. Partial strains on 5 gauges in the mid-plane.

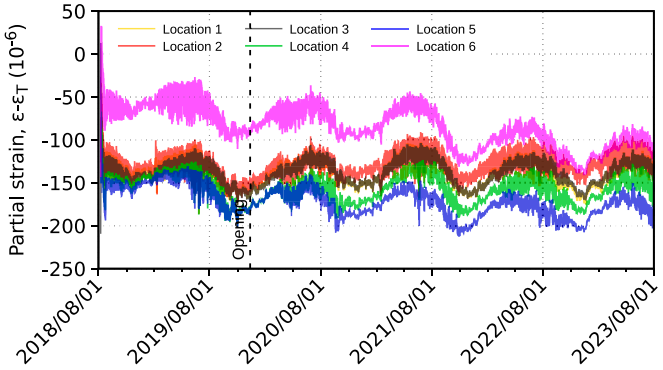

Fig. 8. Partial strains on 6 top gauges located 50 mm under the top surface.

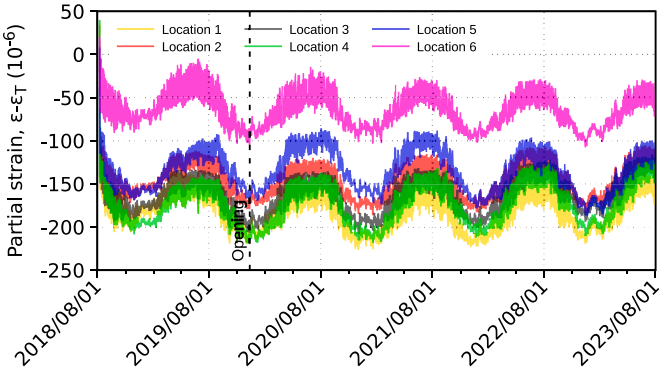

Fig. 9. Partial strains on 6 bottom gauges located 50 mm above the bottom surface.

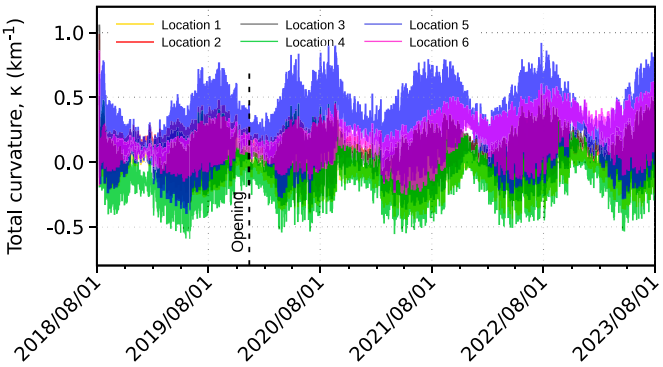

Fig. 10. Total curvatures at six locations.

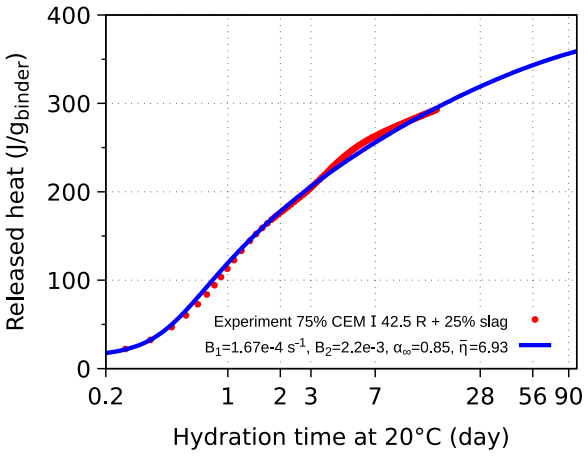

Fig. 11. Results from isothermal calorimetry and calibrated model.

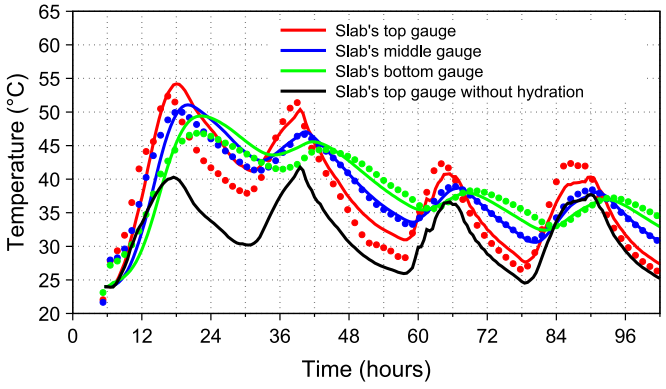

Fig. 12. Temperature validation of the thermal model (lines) against experimental data (points) for the early age. Top, middle and bottom gauges positions are displayed, time 0 represents midnight.

Each location 1–6, see Fig. 4, contains three vibrating wire strain gauges located 50 mm from the surfaces and in the mid-height. All the strain gauges contain integrated temperature sensors. Strain gauges follow orientation of principal strain directions and beyond individual strains they provide average mid-plane strain and curvature.

The measured data are of paramount importance and a brief data summary is provided over the five years of measurement. The temperature profiles resemble 1D heat transport, hence Fig. 5 shows temperatures from only 5 gauges. The maximum measured temperature in the slab reached 52.1 °C after the casting, later the maximum temperatures reached 46.3 °C during summer and −8.2 °C during winter. A linear

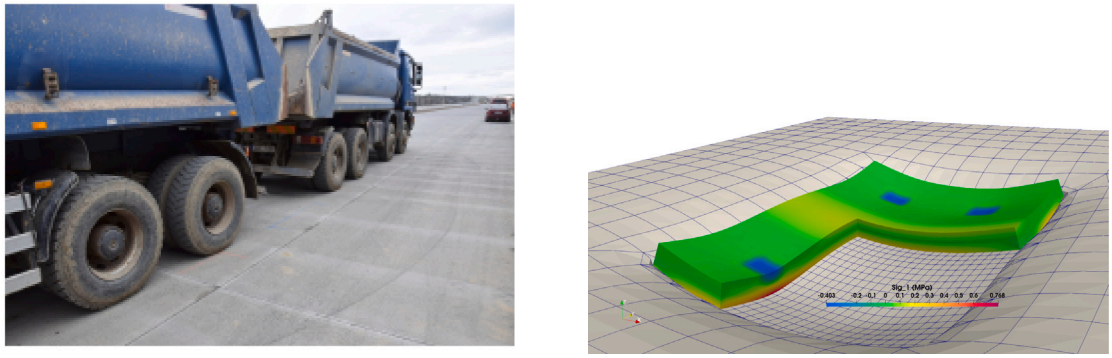

(a) (b)

Fig. 13. Overview of (a) the static load test and (b) numerical solution.

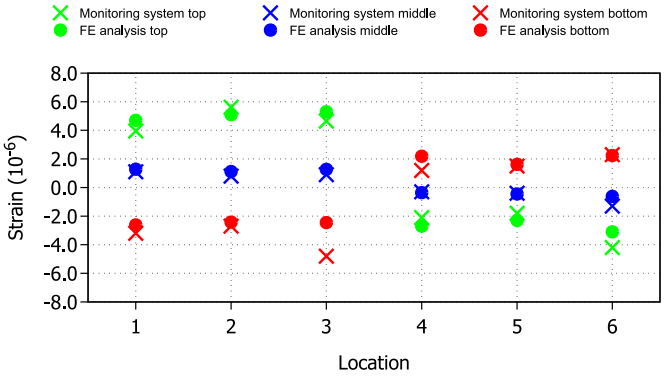

Fig. 14. Validation of the subsoil model with the static load test.

extrapolation to top and bottom surfaces provides extreme values of 49.2 °C and −9.2 °C. Ambient air temperature lies in the range between −17.3 °C and 41.9 °C.

Fig. 6 summarizes the temperature gradient, calculated from the temperature difference and assuming a linear temperature distribution across the thickness. The extreme values beyond the first days are −62 °C/m and 28 °C/m. It is clear that solar radiation causes an additional increase of the surface temperature, leading to approximately a two-times higher negative gradient than the positive one induced by night cooling.

Strain decomposition into different parts allows deducting the temperature effect and defining the partial strain as

$$\varepsilon - \varepsilon_T = \varepsilon_{ve} + \varepsilon_{as} + \varepsilon_{ds} + \varepsilon_f, \tag{15}$$

where the strains correspond to total, thermal, viscoelastic, autogenous shrinkage, drying shrinkage, fracturing strain and possibly other strains. Fig. 7 shows partial strains on the mid-plane, zeroed at 2 hours after the end of setting for all gauges. Autogenous shrinkage plays a dominant role in the first week, reaching $-70 \cdot 10^{-6}$ in the transversal direction at location 6. In the longitudinal directions, continuous casting led to prestressing, which prevented free thermal expansion. A continuous strain drift $-10 \sim -80 \cdot 10^{-6}$ is remarkable over five years, attributed mainly to average drying shrinkage strain. Location 3 was discarded due to inconsistent data. It is interesting to note that the first 16 months there was no public traffic. After the opening, the partial strain shows no abrupt changes in Figs. 7–9, only the effect of drying shrinkage became obvious.

The fluctuations in partial strains depend on deduced thermal strain ε_T. The coefficient of concrete thermal expansion is assumed as $10 \cdot 10^{-6}$ which causes the smallest fluctuations in the partial strain. Annual change in relative humidity is likely the main cause of fluctuations, which is delayed due to slow moisture transport in the slab.

Table 1
Material parameters for static load test analysis.

Material	Thickness (mm)	E (MPa)	ν (–)
Concrete pavement	290	35 000	0.20
Gravel$_{Mzk}$	200	600	0.25
Gravel$_{Sd_A}$	150	400	0.30
Soil	3 000	80	0.35

The measured total strains allowed calculating the total curvature of the slab, assuming a planar deformation of the cross-section. Fig. 10 shows the total curvatures, capturing the temperature variations and demonstrating a slow positive drift due to top drying. Locations 1, 2, 3, 6 show similar curvatures, whereas locations 4, 5 show higher amplitudes since they are located close to the edges. Location 6 provides the largest long-term drift curvature +0.21 km^{-1} over five years corresponding to warping.

3.2. Thermal simulation for the first four days

The simulation covers the early age of the slab, when hydration heat contributes to the temperature rise significantly. Isothermal calorimetry measured the heat release rate and the calibrated affinity hydration model from [40] led to parameters $B_1, B_2, \alpha_\infty, \bar{\eta}$, see Fig. 11 and Table 3. The activation energy E_a was assumed as 38 300 J/mol.

The initial and boundary conditions followed as much real-time data as possible, i.e. solar irradiance, radiation and air temperature convective terms. The heat transfer coefficient h is assumed $h = 10$ W/m^2/K according to [52].

The thermal sub-model validation is shown in Fig. 12 with good results. The maximum temperature reaches 54.2 °C at the top, where the solar irradiance and the hydration heat add together. The maximum error is 4 °C, occurring up to 48 hours. The reason stems likely from higher concrete conductivity at the early age.

The contribution of hydration can be demonstrated on the same model, switching off the heat source $Q(\boldsymbol{x}, t)$ in Eq. (1). The temperature reaches 40.3 °C during the first day and 41.8 °C during the second day after concrete casting. The contribution of hydration to the maximal temperature in the slab is 13.9 °C, see Fig. 12.

3.3. Static load test

The static load test took place on the monitored slab Apr 29, 2019, 7 months after the casting. Two trucks weighing 37.08 and 38.42 t were positioned to induce a concave shape of the slab, see Fig. 13. The axle's load on the slab was 110 kN.

The objectives aimed at finding the subsoil parameters of the Winkler–Pasternak model c_1 and c_2. Due to limited information on

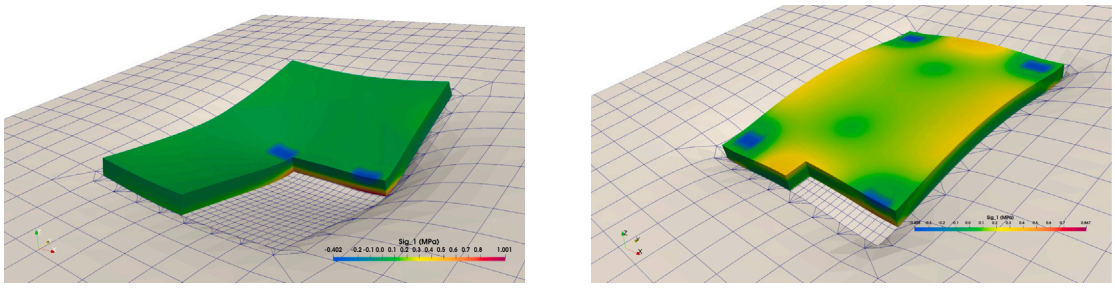

(a) (b)

Fig. 15. Maximal principal tensile stress from traffic loading (a) at the bottom surface and (b) at the top surface of the slab.

shear transfer, a full 3D model of a complete subsoil system was assembled according to Table 1 which provides the thicknesses and elastic properties of used materials largely derived from the TP170 code [53]. Finally, the deformed shape from 3D model was fitted with $c_1 = 70.0$ MNm^{-3} and $c_2 = 60.0$ MNm^{-1} [54], corresponding closely to results in [48].

The calibrated model led to reasonable strain validation in Fig. 14, displayed at all 6 × 3=18 locations of strain gauges. Vibrating strain gauges have strain accuracy around $1 \cdot 10^{-6}$ and the relative error becomes high due to measured low strains. The effect of dowel bars was disregarded since the trucks loaded nearly symmetrically also the neighboring slabs by other axles, yielding low shear force to the dowel bars. The tie bars have 6.25× lower shear stiffness per unit slab length, contributing even less to load distribution. Unfortunately, no direct vertical displacement was measured and the model predicts maximum of 0.26 mm.

In the next step, loading forces (4 forces 50 kN each) were positioned according to Westergaard's approach and according to TP170 [53], mimicking traffic load. They led to maximal values of principal stress on the top and bottom surface. The maximal value of the principal tensile stress on the slab is $\sigma_1 = 1.00$ MPa located on the bottom of the slab, see Fig. 15(a). The maximal value of the principal tensile stress on the top of the slab is $\sigma_{Traffic} = 0.53$ MPa (Fig. 15(b)) with the worst load positions.

3.4. Thermo-mechanical simulation during characteristic summer days

Air temperature and sun irradiation are dominant loads during warm summer days. The analysis for a characteristic winter week was performed and its effect is negligible compared to summer. The thresholded sinusoidal function is suitable for the air temperature and sun irradiation approximation [55], which was calibrated as

$$T_{air}(t) = 10 \cdot \sin\left[\left(\frac{2 \cdot \pi}{86400}\right) \cdot (t - 9 \cdot 3600)\right] + 25, \quad (16)$$

$$q_{e,sun}(t) = 700 \cdot \sin\left[0.85 \cdot \left(\frac{2 \cdot \pi}{86400}\right) \cdot (t - 6 \cdot 3600)\right] \wedge q_{e,sun}(t) \geq 0, \quad (17)$$

where $T_{air}(t)$ is the ambient air temperature and $q_{e,sun}(t)$ is the solar irradiation flux. Both functions are showed graphically in Fig. 16 for a characteristic summer week between Aug 7, 2020 and Aug 15, 2020.

The heat transport model shows very good validation with experimental data for the summer cycle, see Fig. 17(a). The achieved maximal temperature on the slab's top surface is 41.7 °C and the lowest daily value is 24.8 °C, the bottom shows the peak value of 34.3 °C and the lowest value of 29.4 °C. The peaks between the top and the bottom surface are shifted, creating a temperature difference of +9.9 °C and −6.4 °C. The corresponding temperature gradients are + 34.1 °C/m and −22.1 °C/m. The strain validation is shown in Fig. 17(b) at location 3, where the $\Delta\epsilon$ from temperature cycle is presented, instead of absolute strain due to cyclic nature of loading, the model shows good validation to experimental data. The material parameters for MPS model from Table 3 were used, setting $\kappa_T = 0$ due to short-term temperature cycle.

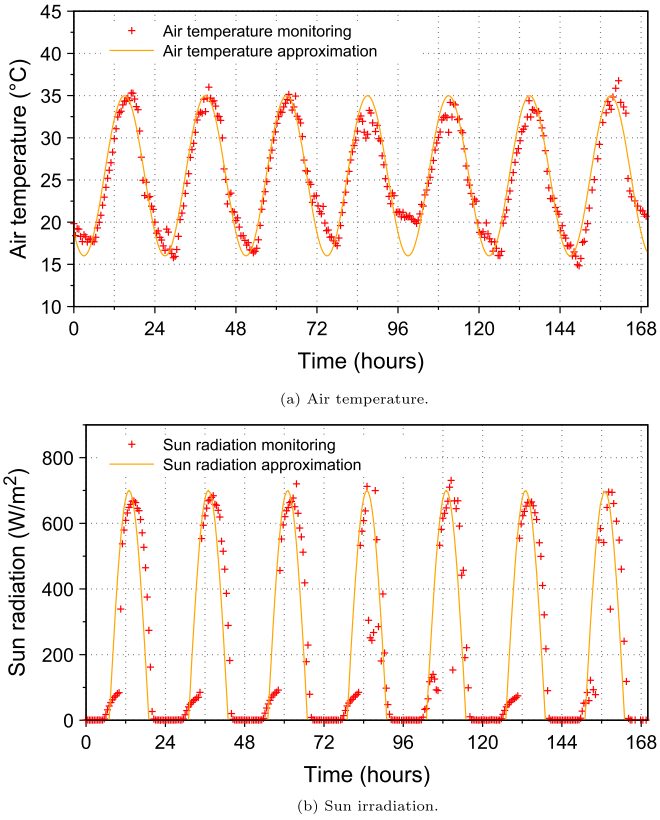

(a) Air temperature.

(b) Sun irradiation.

Fig. 16. Approximations of (a) air temperature and (b) sun irradiation for characteristic summer cycles (time from midnight).

The stress induced by the summer temperature cycle in the pavement slab at 2:00 is shown in Fig. 18(a). On the surface of the slab, there is a significant highest principle tensile stress $\sigma_1 = 1.807$ MPa, corresponding to 40%–50% of the tensile strength. Similar values were found using analytical approach [56]. The compressive stress is negligible $\sigma_3 = -0.569$ MPa.

The second peak stress occurs in the afternoon at 16:30 (Fig. 18(b)), the top surface is compressed with $\sigma_3 = -2.476$ MPa. Maximum principle tensile stress is $\sigma_1 = 1.718$ MPa. The stress acts in opposite way, with the bottom of the slab in tension and the top in compression. Compressive stress values are higher compared to the night time, which is caused by a greater temperature gradient, but the principal tensile stresses have comparable maximal values during the day or at night.

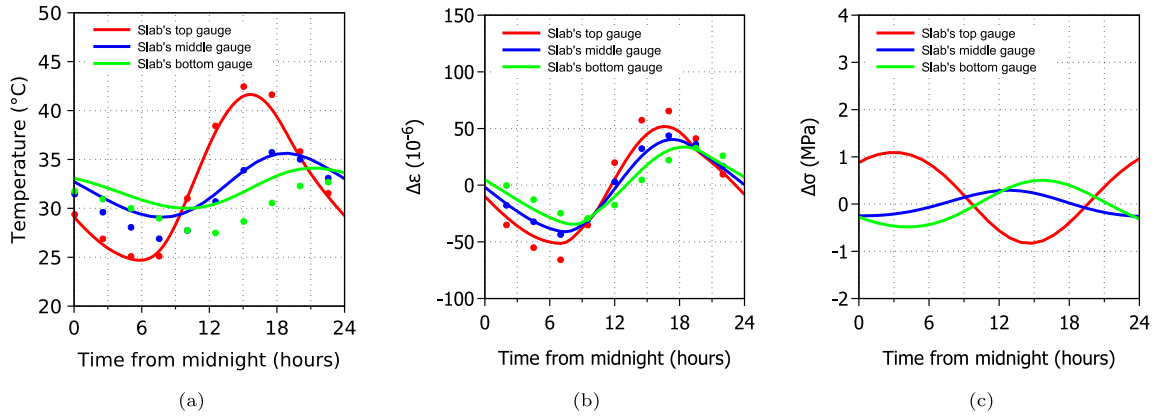

Fig. 17. Validation for a characteristic summer cycle at three height levels (top, center, bottom) at location 3 for (a) temperature, (b) strain difference and (c) the resulting stress.

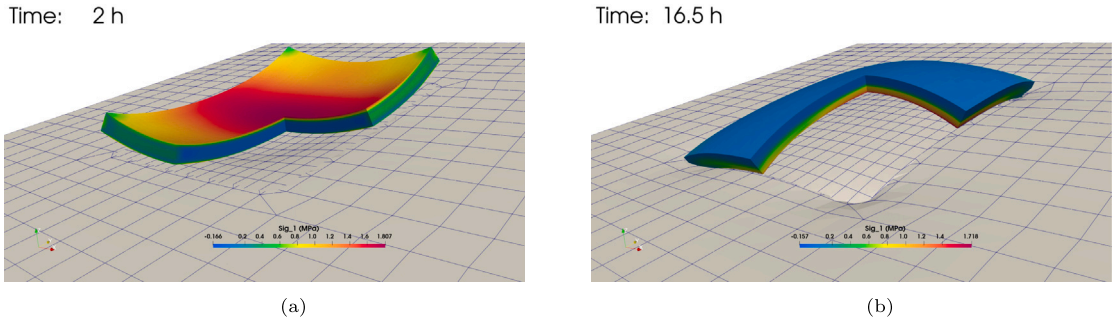

Fig. 18. Temperature induced stress and deformed shape from a summer temperature cycle at (a) 2:00 and (b) at 16:30.

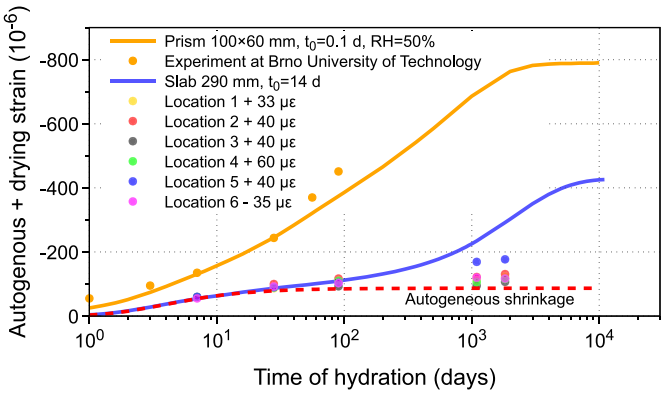

Fig. 19. Shrinkage validation of the concrete pavement slab. The middle strain gauge in Location 3 was discarded and replaced with average value from top and bottom gauges in the same location.

3.5. Hygro-mechanical simulation of long-term drying

Moisture dissipation due to drying is a remarkably slow process. The calibration starts with small lab prisms 60×100×1000 mm made from the same bottom concrete and dried only from the top side 100 × 1000 mm. The ambient air's relative humidity was 0.50 and the drying took 90 days. The permeability c_1 and the hygric exchange coefficient β were calibrated from the moisture transport model, see Fig. 19.

The boundary moisture conditions of the slab are generally unknown, however, they were identified from a 40 years old concrete slab extracted from a similar concrete highway pavement. The thickness of the old slab is only 240 mm compared to 290 mm used in the current simulation. The moisture profile was measured using the Greisinger GMH 3810 resistive material-moisture measuring device, showing a linear profile of relative humidity with 0.65 on the top and 0.80 on the bottom (the moisture profile was scaled from 240 mm to 290 mm), see Fig. 20, the k_1 moisture capacity was also determined from this measurement. The moisture permeability c_1 was set as double according to concrete in the third column in Table 1 [57].

Temporary sealing agents are commonly used for the top slab surface to prevent moisture loss. It is assumed that the agents set $\beta = 0$ kg/(m^2·d) during 14 days after concrete casting and then it completely disappears with $\beta = 0.0459$ kg/(m^2·d). The same moisture transfer coefficients are set for the top and the bottom surfaces. As concrete pavements are externally cured, the β coefficient is decreased. But the duration and the β decrease ratio due to external curing are unclear. The ambient relative humidity was set to 0.65 for the top surface and 0.80 for the bottom surface of the slab. The material parameters for MPS model are summarized in Table 3.

The linear moisture profile from Fig. 20 also implies that the moisture permeability needs to stay constant, otherwise a non-linear asymptotic profile would be obtained. The explanation for this phenomenon is likely a sorption isotherm and resaturation with rain water. It was showed on prisms that rewetting is by orders of magnitude a faster process than drying, thus occasional rain will induce a linear moisture profile [58]. This leads to setting $\alpha_0 = 1$ and $c(h) = c_1$ according to Eq. (6).

The prediction of the calibrated hygro-mechanical model is shown in Fig. 19. The strains from the gauges were shifted to eliminate the early-age longitudinal prestressing effect by 33 ~ 60 ·10^{-6}. The prediction shows that the slab will be drying for approximately 30 years. It should be mentioned that the strain gauges show smaller mid-plane shrinkage, attributed likely to inaccurate moisture profile.

The relative humidity profile across the thickness shows initially a highly nonlinear profile, which becomes linear after approximately 15 years, see Fig. 20. The restrained drying shrinkage induces self-equilibrated normal stress, reaching 3.53 MPa on the top at 60 days, see Fig. 20. In this particular case, $\sigma_x = \sigma_y = \sigma_1$. As the drying front

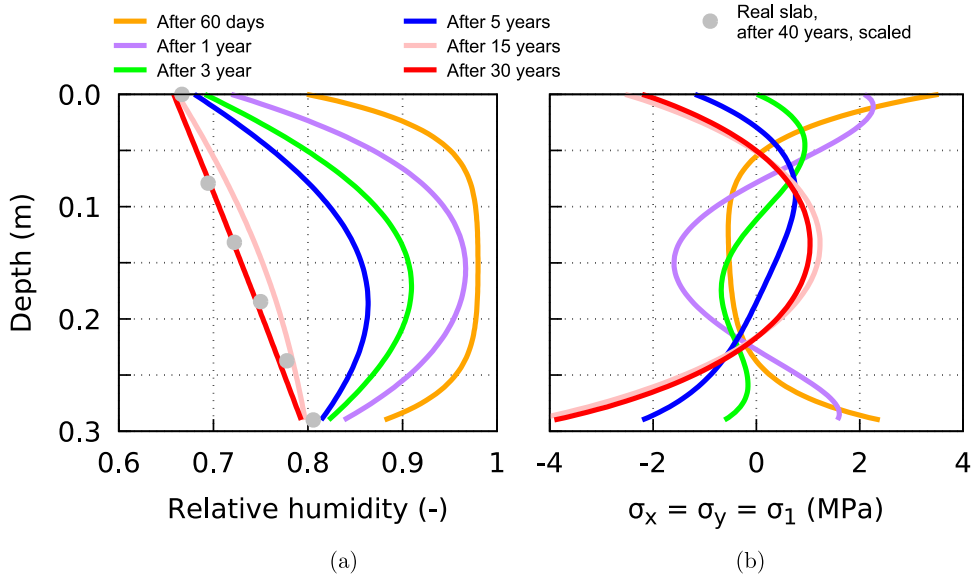

Fig. 20. Comparison of the (a) relative humidity profile from the FE simulation with real slab data after 40 years and (b) stress $\sigma_x = \sigma_y = \sigma_1$ induced by long-term drying.

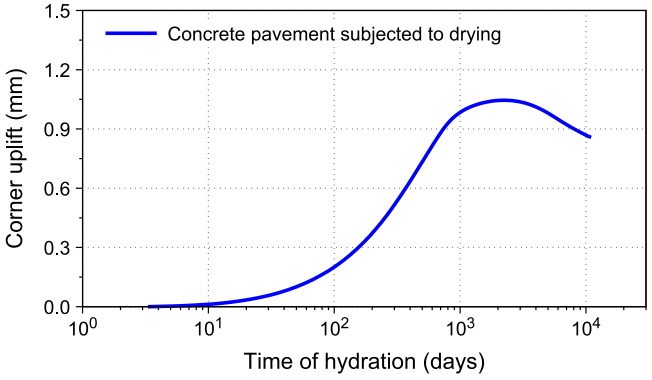

Fig. 21. Warping induced by long-term drying of concrete.

advances, the normal stress at the top decreases to zero at approximately 3 years and yields −2.21 MPa at 30 years. Similar results were found [59]; exposing a 150 mm thick slab to 0.60 RH drying led to tensile stresses up to 3 MPa at 100 days.

The drying of the slab leads to warping, the simulation predicts a maximum corner uplift up to 1.05 mm at 3 years, decreasing further due to creep and advancing drying, see Fig. 21.

3.6. Maximum tensile stresses in the slab

Various loading cases can be superimposed in the framework of linear viscoelastic mechanics, which is used throughout the paper. The maximum principal stress due to drying, summer temperature and traffic is summarized in Table 2, considering the top surface at the center of the slab. The short-term splitting tensile strength of the top concrete was $f_{ctm,sp}$ = 4.2 MPa at 60 days, which is reduced to uniaxial strength and sustained load to approximately $f_{ct} = 0.75 \cdot 4.2 =$ 3.15 MPa [60]. This value is exceeded by sole drying at 60 days and by load combinations up to 3 years.

The consequences are such that drying induces cracking and the cracks propagate up to approximately 5 cm of the pavement slab, deduced from stress profile when exceeding tensile strength. For more detailed propagation and accurate depth prediction of cracking, the incorporation of fracture model is necessary going beyond the objectives of this article. Equilibration of moisture profile closes the cracks after

Table 2
Maximum principal stress on the top surface at location 3 induced by different loading scenarios and their sum.

Maximum first principal stress (MPa) due to				
Concrete age	Drying	Temperature	Traffic	Sum
60 days	3.53	1.81	0.53	5.87
1 year	2.09	1.81	0.53	4.43
3 years	0.12	1.81	0.53	2.46
5 years	−1.19	1.81	0.53	1.15
15 years	−2.54	1.81	0.53	−0.2
30 years	−2.21	1.81	0.53	0.13

approximately three years, however, changes in boundary conditions would promote cracking due to wetting/drying. It is common practice to introduce moisture barriers which slow down drying. Since those barriers are degradable, the onset of cracking can happen later. Mitigation is achievable by crack-resistant cements during drying which is easily facilitated by low reactivity or low Blaine fineness [51]. The accumulation of fatigue damage can be assessed with the Palmgren–Miner rule.

4. Conclusions

This paper analyzes a single concrete pavement slab, subjected to characteristic thermo-hygro-mechanical loading scenarios from casting to long-term drying. Based on the analyses performed in this work, the following conclusions can be drawn:

- A unique monitoring system has been installed, collecting temperature and strain data reliably for over five years, serving for calibration and validation.
- Summer casting led to the maximum slab's concrete temperature of 54.2 °C. The heat of hydration contributed to an increase by 13.9 °C. Low-heat cements and concretes with a low cement dose act beneficially to mitigate the maximum temperature.
- When the slab was subjected solely to characteristic summer temperature cycles, the maximum principal stress attains 1.81 MPa during night cooling.
- Concrete drying induces high tensile stress due to internal restraint. The maximum reaches 3.53 MPa at 60 days on the top surface, decreasing further due to stress relaxation and decreasing moisture gradient. Stresses due to drying are neglected in the majority of design methods.

Table 3
Material input parameters overview.

Moisture transport model					
c_1	0.75 ·10^{-3}	kg/(m·d)	α_0	1.0	–
k_1	160.0	kg/m^3	β	0.0459	kg/(m^2·d)
Heat transport model (with layer thicknesses h)					
$c_{concrete}$	950	J/(kg °C)	$\lambda_{concrete}$	1.9	W/(m °C)
$\rho_{concrete}$	2 400	kg/m^3	$h_{concrete}$	0.29	m
c_{gravel}	700	J/(kg °C)	λ_{gravel}	1.4	W/(m °C)
ρ_{gravel}	1 900	kg/m^3	h_{gravel}	0.35	m
c_{soil}	700	J/(kg °C)	λ_{soil}	1.0	W/(m °C)
ρ_{soil}	1 800	kg/m^3	h_{soil}	5.0	m
Hydration model					
Q_{pot}	430	kJ/kg	m_c	370	kg/m^3
B_1	1.67·10^{-4}	1/s	B_2	2.2·10^{-3}	–
α_∞	0.850	–	$\bar{\eta}$	6.93	–
T_0	25	°C	E_a	38 300	J/mol
λ_0	1.8	W/(m °C)			
Mechanical model					
$\overline{f}_c$	45.0	MPa	c_1	70.0	MNm^{-3}
c_c	370.0	kg/m^3	c_2	60.0	MNm^{-1}
w/c	0.4	–	α	10.0 · 10^{-6}	°C^{-1}
a/c	4.91	–	k	200.0	MNm^{-1}
t_0	7	days	k_3	35	–
k_{sh}	1.5 ·10^{-3}	–	κ_T	0	–
$\epsilon^{\infty}_{sh,au}$	−87.0 ·10^{-6}	–	p	1000	–
τ_{au}	1.05	days	E_{mature}	35.0	GPa
α_{au}	1.166	–	ν	0.2	–
$R_{t,au}$	−4.5	–			

- Combination of drying, temperature and traffic load leads easily to crack formation up to 5 cm deep. Therefore, concrete should be designed as crack-resistant for drying, which can be achieved with slow-hardening binders [51]. Fibers provide another approach to bridge induced cracks [61,62].
- The average drying shrinkage of the slab is over-predicted at five years, attributed likely to an inaccurate moisture profile and boundary conditions.
- The hygro-thermo-mechanical model for a concrete slab can find wide application in more accurate design or in fatigue analysis. Extension with fracture models can predict crack induction and propagation, in dependence on various geometry and boundary conditions and optimize the casting process, curing and maintenance of concrete pavements.

CRediT authorship contribution statement

Jakub Veselý: Validation, Formal analysis, Investigation, Resources, Writing – original draft, Visualization. **Vít Šmilauer:** Conceptualization, Writing – review & editing, Supervision, Funding acquisition.

Declaration of competing interest

The authors declare that they have no known competing financial interests or personal relationships that could have appeared to influence the work reported in this paper.

Data availability

Publicly available data are shared at Zenodo repository (doi.org/10.5281/zenodo.7534928) and on Mendeley data (http://dx.doi.org/10.17632/4kmfsjz5p7.1).

Hygro-thermo-mechanical model for concrete pavement from an early age to a long-term performance (Original data) (Mendeley Data)

Acknowledgments

We acknowledge financial support for this work from the Czech Science Foundation under the project number 21-03118S. Dr. B. Slánský and L. Vysloužil from Skanska a.s. company are acknowledged for their valuable insights and contributions to the long-term monitoring system. Credits belong also to The Road and Motorway Directorate of the Czech Republic who supported the idea of detailed slab monitoring and coordinated the installation.

References

[1] M.G. Lay, Handbook of Road Technology, CRC Press, 2009.
[2] T. Gasch, R. Malm, A. Ansell, A coupled hygro-thermo-mechanical model for concrete subjected to variable environmental conditions, Int. J. Solids Struct. 91 (2016) 143–156, http://dx.doi.org/10.1016/j.ijsolstr.2016.03.004, https://www.sciencedirect.com/science/article/pii/S0020768316001232.
[3] M. Nehdi, A.M. Soliman, Early-age properties of concrete: Overview of fundamental concepts and state-of-the-art research, Proc. Inst. Civ. Eng. Constr. Mater. 164 (2) (2011) 57–77, http://dx.doi.org/10.1680/coma.900040.
[4] A. Mateos, J. Harvey, J. Bolander, R. Wu, J. Paniagua, F. Paniagua, Structural response of concrete pavement slabs under hygrothermal actions, Constr. Build. Mater. 243 (2020) 118261, http://dx.doi.org/10.1016/j.conbuildmat.2020.118261, https://www.sciencedirect.com/science/article/pii/S095006182030266X.
[5] D.P. Bentz, A review of early-age properties of cement-based materials, Cem. Concr. Res. 38 (2) (2008) 196–204, http://dx.doi.org/10.1016/j.cemconres.2007.09.005, https://www.sciencedirect.com/science/article/pii/S0008884607002165. Special Issue — The 12th International Congress on the Chemistry of Cement. Montreal, Canada, July 8–13 2007.
[6] A.A. Chiniforush, M. Gharehchaei, A. Akbar Nezhad, A. Castel, F. Moghaddam, L. Keyte, D. Hocking, S. Foster, Numerical simulation of risk mitigation strategies for early-age thermal cracking and DEF in concrete, Constr. Build. Mater. 322 (2022) 126478, http://dx.doi.org/10.1016/j.conbuildmat.2022.126478, https://www.sciencedirect.com/science/article/pii/S0950061822001702.
[7] D. Smiley, W. Hansen, et al., Investigation of Early Cracking on Selected JPCP Projects, Tech. Rep., Michigan. Dept. of Transportation. Construction and Technology Division, 2007.
[8] J. Yang, Y. Guo, A. Shen, Z. Chen, X. Qin, M. Zhao, Research on drying shrinkage deformation and cracking risk of pavement concrete internally cured by SAPs, Constr. Build. Mater. 227 (2019) 116705, http://dx.doi.org/10.1016/j.conbuildmat.2019.116705, https://www.sciencedirect.com/science/article/pii/S0950061819321233.
[9] J. Chen, H. Wang, P. Xie, Pavement temperature prediction: Theoretical models and critical affecting factors, Appl. Therm. Eng. 158 (2019) 113755, http://dx.doi.org/10.1016/j.applthermaleng.2019.113755, https://www.sciencedirect.com/science/article/pii/S1359431118377974.
[10] M. Li, W. Xu, Y. Wang, Q. Tian, J. Liu, Shrinkage crack inhibiting of cast in situ tunnel concrete by double regulation on temperature and deformation of concrete at early age, Constr. Build. Mater. 240 (2020) 117834, http://dx.doi.org/10.1016/j.conbuildmat.2019.117834, https://www.sciencedirect.com/science/article/pii/S0950061819332878.
[11] J. Xin, G. Zhang, Y. Liu, Z. Wang, Z. Wu, Effect of temperature history and restraint degree on cracking behavior of early-age concrete, Constr. Build. Mater. 192 (2018) 381–390, http://dx.doi.org/10.1016/j.conbuildmat.2018.10.066, https://www.sciencedirect.com/science/article/pii/S0950061818324632.
[12] K.C. Mahboub, Y. Liu, D.L. Allen, Evaluation of temperature responses in concrete pavement, J. Transp. Eng. 130 (3) (2004) 395–401, http://dx.doi.org/10.1061/(ASCE)0733-947X(2004)130:3(395).
[13] A.M. Ioannides, Concrete pavement analysis: The first eighty years, Int. J. Pavement Eng. 7 (4) (2006) 233–249, http://dx.doi.org/10.1080/10298430600798481.
[14] H.M. Westergaard, Stresses in concrete pavements computed by theoretical analysis, Public Roads (1926).
[15] H.M. Westergaard, Analysis of stresses in concrete pavements due to variations of temperature, in: Highway Research Board Proceedings, vol. 6, 1927.
[16] Y. Sun, Z. Zheng, W. Huang, J. Wang, Analytical solution based on state-space method for cracked concrete pavement subjected to arbitrary concentrated loading, Constr. Build. Mater. 347 (2022) 128612, http://dx.doi.org/10.1016/j.conbuildmat.2022.128612, https://www.sciencedirect.com/science/article/pii/S0950061822022693.
[17] Y.H. Huang, S.T. Wang, Finite-element analysis of concrete slabs and its implications for rigid pavement design, Highw. Res. Rec. (466) (1973).

[18] G.T. Korovesis, Analysis of Slab-on-Grade Pavement Systems Subjected to Wheel and Temperature Loadings (Ph.D. thesis), University of Illinois at Urbana-Champaign, 1990.
[19] B. Choubane, M. Tia, Nonlinear temperature gradient effect on maximum warping stresses in rigid pavements, Transp. Res. Rec. 1370 (1) (1992) 11.
[20] A.M. Tabatabaie, E.J. Barenberg, Finite-element analysis of jointed or cracked concrete pavements, Transp. Res. Rec. (671) (1978).
[21] Y.T. Chou, Structural Analysis Computer Programs for Rigid Multicomponent Pavement Structures with Discontinuities–WESLIQID and WESLAYER. Report 1. Program Development and Numerical Presentations, Tech. Rep., Army Engineer Waterways Experiment Station Vicksburg MS Geotechnical Lab, 1981.
[22] S.D. Tayabji, B.E. Colley, Improved rigid pavement joints, Transp. Res. Rec. 630 (1983) 69–78.
[23] Y.H. Huang, Pavement Analysis and Design, Prentice Hall, 1993, https://books.google.cz/books?id=OjRSAAAAMAAJ.
[24] B.H. Al-Humeidawi, P. Mandal, Numerical evaluation of the combined effect of dowel misalignment and wheel load on dowel bars performance in JPCP, Eng. Struct. 252 (2022) 113655, http://dx.doi.org/10.1016/j.engstruct.2021.113655, https://www.sciencedirect.com/science/article/pii/S0141029621017442.
[25] V. Sadeghi, S. Hesami, Investigation of load transfer efficiency in jointed plain concrete pavements (JPCP) using FEM, Int. J. Pavement Res. Technol. 11 (3) (2018) 245–252, http://dx.doi.org/10.1016/j.ijprt.2017.10.001, https://www.sciencedirect.com/science/article/pii/S1996681417300135.
[26] Y. Dere, A. Asgari, E.D. Sotelino, G.C. Archer, Failure prediction of skewed jointed plain concrete pavements using 3D FE analysis, Eng. Fail. Anal. 13 (6) (2006) 898–913, http://dx.doi.org/10.1016/j.engfailanal.2005.07.001, https://www.sciencedirect.com/science/article/pii/S1350630705001494.
[27] P. Mackiewicz, Thermal stress analysis of jointed plane in concrete pavements, Appl. Therm. Eng. 73 (1) (2014) 1169–1176, http://dx.doi.org/10.1016/j.applthermaleng.2014.09.006, https://www.sciencedirect.com/science/article/pii/S1359431114007789.
[28] L. Bronuela, H.D. Lee, S. Ryu, Y.H. Cho, Cantilever and pull-out tests and corresponding FEM models of various dowel bars in airport concrete pavement, Constr. Build. Mater. 83 (2015) 181–188, http://dx.doi.org/10.1016/j.conbuildmat.2015.02.066, https://www.sciencedirect.com/science/article/pii/S0950061815002172.
[29] K. Singh, G. Ghosh, Stress behavior of concrete pavement, Mater. Today: Proc. (2021) http://dx.doi.org/10.1016/j.matpr.2021.06.424, https://www.sciencedirect.com/science/article/pii/S2214785321048185.
[30] Z. Lyu, Y. Guo, Z. Chen, A. Shen, X. Qin, J. Yang, M. Zhao, Z. Wang, Research on shrinkage development and fracture properties of internal curing pavement concrete based on humidity compensation, Constr. Build. Mater. 203 (2019) 417–431, http://dx.doi.org/10.1016/j.conbuildmat.2019.01.115, https://www.sciencedirect.com/science/article/pii/S0950061819301412.
[31] X. Zhang, H. Zhao, Characterization of moisture diffusion in cured concrete slabs at early ages, Adv. Mater. Sci. Eng. 2015 (2015).
[32] J.-H. Jeong, D.G. Zollinger, Environmental effects on the behavior of jointed plain concrete pavements, J. Transp. Eng. 131 (2) (2005) 140–148, http://dx.doi.org/10.1061/(ASCE)0733-947X(2005)131:2(140).
[33] S. Liang, Y. Wei, Z. Wu, W. Hansen, Performance evaluation of concrete pavement slab considering creep effect by finite element analysis, Transp. Res. Rec. 2672 (27) (2018) 65–77, http://dx.doi.org/10.1177/0361198118772951.
[34] D. Gawin, F. Pesavento, B.A. Schrefler, Hygro-thermo-chemo-mechanical modelling of concrete at early ages and beyond. Part I: Hydration and hygro-thermal phenomena, Int. J. Numer. Methods Eng. 67 (3) (2006) 299–331.
[35] D. Gawin, F. Pesavento, B.A. Schrefler, Hygro-thermo-chemo-mechanical modelling of concrete at early ages and beyond. Part II: Shrinkage and creep of concrete, Int. J. Numer. Methods Eng. 67 (3) (2006) 332–363.
[36] L. Jendele, V. Šmilauer, J. Červenka, Multiscale hydro-thermo-mechanical model for early-age and mature concrete structures, Adv. Eng. Softw. 72 (2014) 134–146.
[37] F. Kanavaris, C. Ferreira, C. Sousa, M. Azenha, Thermo-chemo-hygro-mechanical simulation of the restrained shrinkage ring test for cement-based materials under distinct drying conditions, Constr. Build. Mater. 294 (2021) 123600, http://dx.doi.org/10.1016/j.conbuildmat.2021.123600, https://www.sciencedirect.com/science/article/pii/S095006182101360X.
[38] W. Dong, C. Liu, X. Bao, T. Xiang, D. Chen, Advances in the deformation and failure of concrete pavement under coupling action of moisture, temperature, and wheel load, Materials 13 (23) (2020) http://dx.doi.org/10.3390/ma13235530.
[39] V. Malárics, H.S. Müller, Numerical investigations on the deformation behavior of concrete pavements, in: 7th RILEM International Conference on Cracking in Pavements, Springer, 2012, pp. 507–516.
[40] B. Patzák, OOFEM Project Home Page, Tech. Rep., CTU in Prague, Faculty of Civil Engineering, Prague, 2000, http://www.oofem.org.
[41] H.-G. Kwak, S.-J. Ha, J.-K. Kim, Non-structural cracking in RC walls: Part I. Finite element formulation, Cem. Concr. Res. 36 (4) (2006) 749–760, http://dx.doi.org/10.1016/j.cemconres.2005.12.001, https://www.sciencedirect.com/science/article/pii/S0008884605003091.
[42] F. Pesavento, A. Knoppik, V. Šmilauer, M. Briffaut, P. Rossi, Numerical modelling, in: Thermal Cracking of Massive Concrete Structures, Springer, 2019, pp. 181–255.
[43] M. Jirásek, P. Havlásek, Microprestress-solidification theory of concrete creep: Reformulation and improvement, Cem. Concr. Res. 60 (2014) 51–62.
[44] Z.P. Bažant, S. Baweja, Short form of creep and shrinkage prediction model B3 for structures of medium sensitivity, Mater. Struct. 29 (1996) 587–593.
[45] P. Havlásek, M. Jirásek, Multiscale modeling of drying shrinkage and creep of concrete, Cem. Concr. Res. 85 (2016) 55–74, http://dx.doi.org/10.1016/j.cemconres.2016.04.001.
[46] RILEM Technical Committee TC-242-MDC (Z.P. Bažant, chair), Model B4 for creep, drying shrinkage and autogenous shrinkage of normal and high-strength concretes with multi-decade applicability, Mater. Struct. 48 (2015) 753–770.
[47] A.C. Lamprea-Pineda, D.P. Connolly, M.F.M. Hussein, Beams on elastic foundations – A review of railway applications and solutions, Transp. Geotech. 33 (2022) 100696, http://dx.doi.org/10.1016/j.trgeo.2021.100696, https://www.sciencedirect.com/science/article/pii/S2214391221001860.
[48] B. Breeveld, Modelling the Interaction Between Structure and Soil for Shallow Foundations-a Computational Modelling Approach (Ph.D. thesis), Delft University of Technology, 2013.
[49] D. Younesian, A. Hosseinkhani, H. Askari, E. Esmailzadeh, Elastic and viscoelastic foundations: A review on linear and nonlinear vibration modeling and applications, Nonlinear Dynam. 97 (1) (2019) 853–895.
[50] B. Slánský, V. Šmilauer, J. Hlavatý, R. Dvořák, New long-life concrete pavements in the Czech Republic, in: 12th International Conference on Concrete Pavements, International Society for Concrete Pavements, 2021.
[51] V. Šmilauer, P. Reiterman, R. Šulc, P. Schořík, Crack-resistant cements under drying: Results from ring shrinkage tests and multi-physical modeling, Materials 15 (12) (2022) http://dx.doi.org/10.3390/ma15124040.
[52] Y. Lee, M.-S. Choi, S.-T. Yi, J.-K. Kim, Experimental study on the convective heat transfer coefficient of early-age concrete, Cem. Concr. Compos. 31 (1) (2009) 60–71, http://dx.doi.org/10.1016/j.cemconcomp.2008.09.009, https://www.sciencedirect.com/science/article/pii/S0958946508001212.
[53] J. Kudrna, M. Varaus, F. Luxemburg, L. Vébr, I. Racek, J. Fiedler, A. Arťušenko, NavrhováníVozovek PozemníCh Komunikací, TP170, Tech. Rep., Ministerstvo dopravy, 2004, p. 104.
[54] J. Veselý, V. Šmilauer, Thermo-mechanical model for concrete pavement, Acta Polytech. CTU Proc. 30 (2021) 121–125, http://dx.doi.org/10.14311/APP.2021.30.0121, https://ojs.cvut.cz/ojs/index.php/APP/article/view/7222.
[55] Y. Qin, J.E. Hiller, Modeling temperature distribution in rigid pavement slabs: Impact of air temperature, Constr. Build. Mater. 25 (9) (2011) 3753–3761, http://dx.doi.org/10.1016/j.conbuildmat.2011.04.015, https://www.sciencedirect.com/science/article/pii/S0950061811001553.
[56] S.M. Abraham, G.D.R.N. Ransinchung, Temperature variation and stresses in unreinforced concrete pavement containing RAP, Constr. Build. Mater. 263 (2020) 120506, http://dx.doi.org/10.1016/j.conbuildmat.2020.120506.
[57] Z.P. Bažant, L.J. Najjar, Drying of concrete as a nonlinear diffusion problem, Cem. Concr. Res. 1 (5) (1971) 461–473, http://dx.doi.org/10.1016/0008-8846(71)90054-8.
[58] L. Dohnalová, P. Havlásek, V. Šmilauer, Behavior of predried mature concrete beams subject to partial wetting and drying cycles, Acta Polytech. CTU Proc. 34 (2022).
[59] J. Gomes, R. Carvalho, C. Sousa, J. Granja, R. Faria, D. Schlicke, M. Azenha, 3D numerical simulation of the cracking behaviour of a RC one-way slab under the combined effect of thermal, shrinkage and external loads, Eng. Struct. 212 (2020) 110493, http://dx.doi.org/10.1016/j.engstruct.2020.110493, https://www.sciencedirect.com/science/article/pii/S014102961932601X.
[60] E.M.R. Fairbairn, M. Azenha, S. Asamoto, Y. Ballim, F. Benboudjema, M. Briffaut, J. Carette, et al., Thermal Cracking of Massive Concrete Structures, RILEM State-of-the-Art Reports, Springer, 2019.
[61] B.H. Cho, B.H. Nam, Concrete composites reinforced with graphene oxide nanoflake (GONF) and steel fiber for application in rigid pavement, Case Stud. Constr. Mater. 17 (2022) e01346, http://dx.doi.org/10.1016/j.cscm.2022.e01346, https://www.sciencedirect.com/science/article/pii/S2214509522004788.
[62] O. Ozturk, N. Ozyurt, Sustainability and cost-effectiveness of steel and polypropylene fiber reinforced concrete pavement mixtures, J. Clean. Prod. 363 (2022) 132582, http://dx.doi.org/10.1016/j.jclepro.2022.132582, https://www.sciencedirect.com/science/article/pii/S0959652622021825.